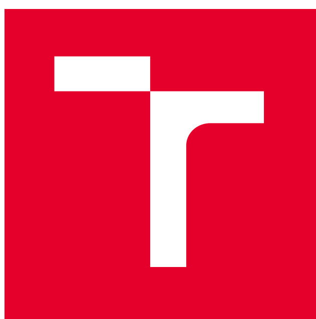

BRNO UNIVERSITY OF TECHNOLOGY

VYSOKÉ UČENÍ TECHNICKÉ V BRNĚ

FACULTY OF MECHANICAL ENGINEERING

FAKULTA STROJNÍHO INŽENÝRSTVÍ

INSTITUTE OF PHYSICAL ENGINEERING

ÚSTAV FYZIKÁLNÍHO INŽENÝRSTVÍ

DEFECTOSCOPY OF THIN POLYMER LAYERS USING COMPUTER VISION

DEFEKTOSKOPIE TENKÝCH POLYMERNÍCH VRSTEV ZA POMOCI POČÍTAČOVÉHO VIDĚNÍ

BACHELOR'S THESIS

BAKALÁŘSKÁ PRÁCE

AUTHOR Jáchym Podstránský

AUTOR PRÁCE

SUPERVISOR Ing. Alexandr Knápek, Ph.D.

VEDOUCÍ PRÁCE

BRNO 2022

Abstrakt

Při procesu elektronové litografie jedním z prvních kroků je ovrstvování substrátu, waferu, tenkou vrstvou polymerního rezistu. V průběhu ovrstvování dochází k defektům, které mohou ovlivňovat expozici a tudíž i funkčnost finální nanostruktury. Kontrolou kvality naneseného rezistu před expozicí je možně se těmto místům s defekty vyhnout. Tento proces je možné provádět ručně pomocí světelného mikroskopu, ale je to časově náročný proces. V rámci této bakalářské práce vzniklo zařízení, které tyto defekty dokáže určit automaticky.

Jde o rastrovací zařízení, které díky kombinaci dvou krokových motorů a optické kamery pořídí snímky požadované oblasti waferu a ty poté za pomoci umělé inteligence zanalyzuje. Uživateli je poté poskytnut dokument v kterém je zapsána velikost, pozice a typ každého z nalezených defektů.

Summary

In the electron beam lithography process, one of the first steps is to coat the substrate, the wafer, with a thin layer of polymer resist. During the coating process, defects occur that can affect the exposure and therefore the functionality of the final nanostructure. By checking the quality of the deposited resin prior to exposure, these defect sites can be avoided. This process can be done manually using a light microscope, but it is a time consuming process. In the framework of this bachelor thesis, a device has been developed that can detect these defects automatically.

It is a rasterising device that, by combining two stepper motors and an optical camera, takes images of the desired area of the wafer and then analyses these with the help of artificial intelligence. The user is then provided with a document in which the size, position and type of each defect found is recorded.

Klíčová slova

defekty v rezistu, umělá inteligence, zpracování obrazu, automatizace

Keywords

defects in resist, artificial intelligence, image processing, automatization

PODSTRÁNSKÝ, J. *Defektoskopie tenkých polymerních vrstev za pomoci počítačového vidění.* Brno: Vysoké učení technické v Brně, Fakulta strojního inženýrství, 2022. 41 s. Vedoucí práce Ing. Alexandr Knápek, Ph.D.

I hereby declare to have written this thesis on my own, under the supervision of Ing. Alexandr Knápek, Ph.D., my bachelor's thesis supervisor. I have used no other resources except those cited and mentioned in the references.

Jáchym Podstránský

My thanks go especially to the family. If it weren't for them, I wouldn't have been able to stay at BUT. Second, also a huge thanks goes to the EBL team from UPT for great support during the development of the system, most notably Ing. Alexandr Knápek, Ph.D., Ing. Milan Matějka, Ph.D., Bc. Jana Chlumská and Mr. Král. Lastly, I would like to thank Ing. Mojmír Šerý, Ph.D. for his urgency and helpfulness.

Jáchym Podstránský

Contents

1 Introduction 3

2 Theoretical Part 5
2.1 Electron resists . . . 5
2.2 Resist deposition method . . . 5
2.3 Optical and mechanical properties of thin layers . . . 7
2.4 Defects in resist layers . . . 8
2.5 Inspection of resist layers . . . 10
2.5.1 The Scanning Electron Microscopy . . . 10
2.5.2 The Atomic Force Microscopy . . . 10
2.5.3 The Visible Light Microscopy . . . 11

3 Measurements and results 13
3.1 Hardware design . . . 13
3.1.1 Mechanical parts . . . 13
3.1.2 Electronics . . . 14
3.1.3 Optics . . . 15
3.2 Algorithmization . . . 17
3.2.1 Communication . . . 17
3.2.2 The graphical user interface . . . 18
3.2.3 Initial process . . . 20
3.2.4 Scanning process . . . 20
3.2.5 Image processing . . . 21
3.3 Measurements . . . 24
3.3.1 Comparison of the manual method with software . . . 24
3.3.2 Consistency and efficiency . . . 25
3.3.3 Improvement of the measurement . . . 27
3.3.4 The effect of ambient light on the measurement . . . 29

4 Conclusions 31

Conclusions 31

Bibliography 33

List of Symbols, Physical Constants, and Abbreviations 37

List of Tables 39

List of Figures **41**

1. Introduction

Electron beam lithography (EBL) is a process that is implemented in nanofabrication for patterning mesoscopic structures or systems with unique advantages of high resolution, high accuracy in positioning, high reliability in processing, and high flexibility in patterning replication. This process is most often done on a silicon wafer. Nowadays, resolution capability is as good as sub 10 nm [1].

The whole process consists of multiple steps. The ain focus is on resist layer deposition and its perfection. It is one of the initial steps, and the most crucial one to get the desired pattern. This step is most often executed, even in laboratories of the Institute of Scientific Instruments of the Czech Academy of Sciences (ISI CAS), by means of spin-coating. During the deposition of resist by spin-coating, various defects can occur: dust contamination, micro-bubbles, bumps, craters, comets, thickness inhomogeneity, etc. [2] [3].

Nowadays, the process of detecting these defects in the resist is done manually under a visible-light microscope (Figure 1.1). The scientist measures it in rows at 3mm intervals in a controlled area of about 50 mm × 50 mm. Every defect that is found is measured, given coordinates and written in a chart. Due to the preciseness and the scale of this work, every wafer takes a dozen of minutes to be inspected. Moreover, the combination of a loosely setted wafer and the possibility of human error can lead to low accuracy of the measurement. Due to this inefficiency of inspection process, a project leading to automate this procedure was assigned. This thesis describes the theory, the development, and the results of the WaferScan instrument. This instrument is designed to semi-automate the process of scanning thin polymer layers for defects using computer vision.

The first part of this bachelor's thesis, the Chapter 2, focuses on already mentioned resist as it is the main component that is being researched. More specifically, it focuses on resists optical, mechanical, and chemical properties, the method of their deposition, the types of defects that can be found in resists, and a description of what microscopy methods can be used to inspect layers of resists.

The second part, the Chapter 3, entails hardware implementation which consists of an engineering and an electrotechnical part. The engineering solution requires a precise design in a clean room, with a sufficiently rigid construction and a range of motion sufficient for measured wafers. The electrotechnical solution requires to work with a micro-controller board, to choose the right motors and optical devices that will allow to take pictures with sufficient resolution. The chapter also describes the software solution, which includes the entire scanning process, the user environment,

and additional features that make it easier for the user to work with the data.

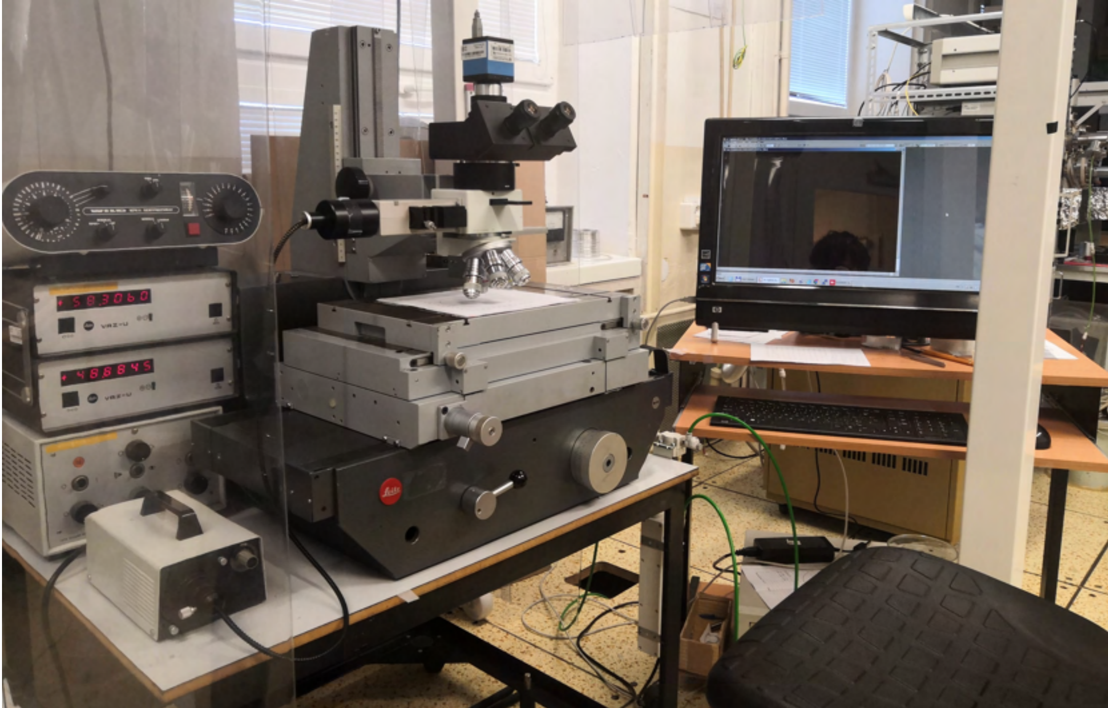

Figure 1.1: The manual setup for the inspection of the defects used in ISI CAS

2. Theoretical Part

2.1 Electron resists

The main property of the resists is the reactivity on an impact of electrons. After the impact, a small area of the resist changes its molar weight. Due to this property, types of resists can be divided in two groups, positive and negative resists [4].

Positive resists have a negative change of their molar weight ΔM after the impact. This leads to a faster dissolution of a irradiated part of the resist. The most common positive resist used in EBL is polymethyl methacrylate in short PMMA. Its most common reaction to an impact of an electron is the breaking of the main chain (Figure 2.1). PMMA is capable to have a resolution smaller than 10 nm [5][6], is very stable under the effect of UV radiation, can withstand temperatures as high as 100 °C, and has a great adhesive property.

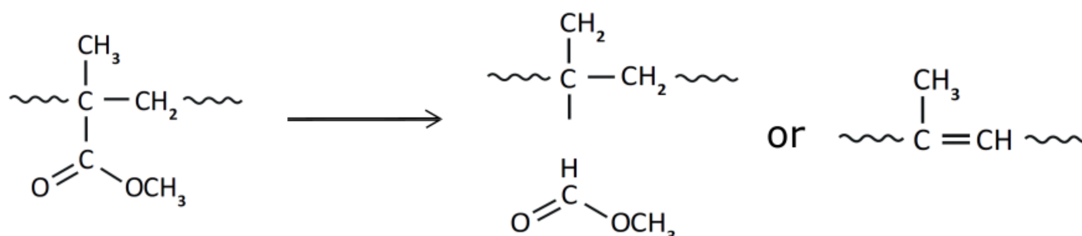

Figure 2.1: A schematic diagram for one repeat unit of PMMA and one of its generic reaction path [7].

For negative resists, a change of molar weight ΔM is positive. This means that the part that is irradiated with electrons dissolves easier. In this group, copolymer of glycidyn methacrylate and ethyl acrylate (COP) are most often used [8].

2.2 Resist deposition method

Spin coating is one of the industry-leading methods of depositing a thin film of material onto a functional substrate. It is a technique that allows us to produce uniform, adherent thin resist films with a thickness of the order of nanometers [9].

For deposition, a substrate mixture of a resist with solvent and a spin coater are regularly used. It is common for the vendor to supply all specific resist data in the data sheet because recommended solvents and their concentrations vary from resist to resist.

The first step of the process is to attach the wafer with vacuum to the rotor, seal the spin coater and start spinning slowly at a spin speed of approximately $500\,\mathrm{min}^{-1}$. The deposition of the solution in the center of a substrate follows. After a full distribution of solvent on the wafer is achieved, the spin speed can be increased. The value at which the spin speed is set obtains a specific thickness of deposited solution w. The function can be described by the following formula [4]:

$$w = k_\eta(c^2\omega^{-1/2}), \tag{2.1}$$

where c is concentration of the solution, ω is the spin speed, and k_η is a constant that includes viscosity and parameters of the spin coater.

After the spin coating is done, soft-baking follows. This process is necessary to get rid of the solvent that helped with the adhesion of the resist. Solvents have a lower evaporating temperature. Due to that a hotplate or a temperature chamber is used. The mentioned data sheets describe the temperature at which the deposited wafer is to be maintained and for how long. For example, the manufacturer MicroChem recommends for their PMMA resist a heating time of 3 minutes at a constant temperature of 180 °C if using hotplate and half an hour at a constant temperature of 170 °C if using a temperature chamber [10].

If both processes are performed without any errors, the final wafer should be homogeneously deposited and free of any defects as in Figure 2.2.

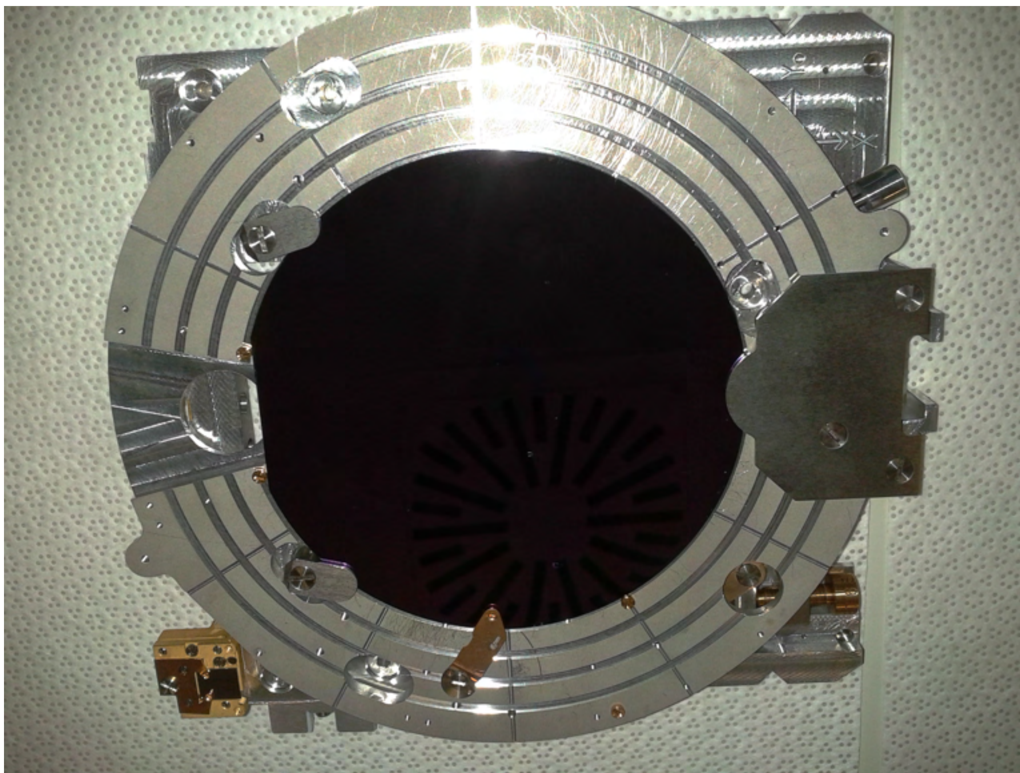

Figure 2.2: A wafer with a PMMA film layer, with an approval from Ing. Stanislav Krátký, Ph.D.

2.3 Optical and mechanical properties of thin layers

On the wafers with applied resist, interference very often can be seen (Figure 2.3). These effects are determined by the optical path length l through the thin PMMA film in a phenomenon called thin-film interference. The optical path length can be calculated easily from [2]:

$$l = n \cdot d, \tag{2.2}$$

where n is the index of refraction of the medium through which light propagates, and d is the length of the path that the light takes through the layer.

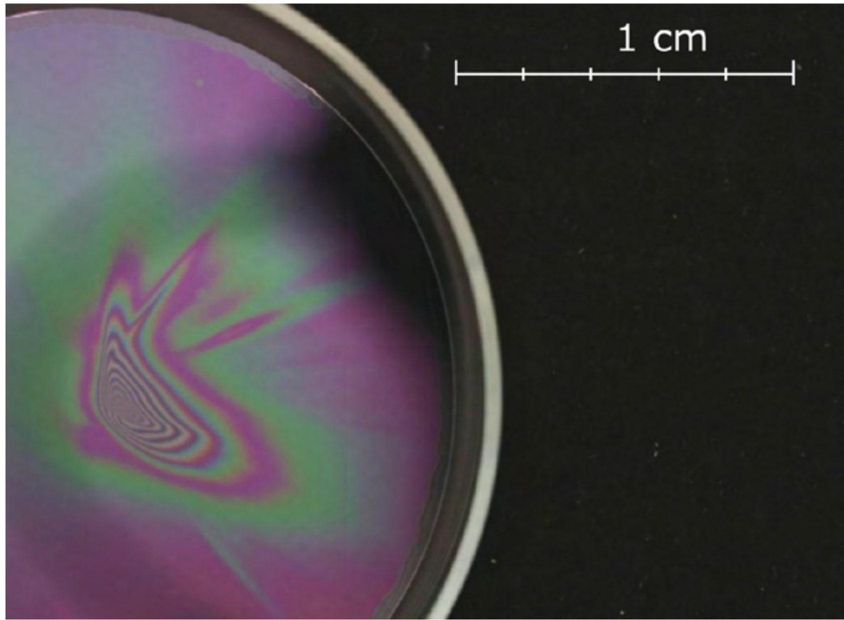

Figure 2.3: A wafer with an inhomogenous film of resist [2]

From reports of Lalova, [11] the index of refraction depends on the thickness of the film. The refractive index n, the extinction coefficient k, and the thickness d of the spin-coated PMMA films deposited on a silicon wafer were determined by using the minimization of a function. The function consists of the discrepancies between measured and calculated R spectra by means of multiwavelength nonlinear curve fitting. The refractive index was described using Sellmeier's equation in the following form:

$$n^2(\lambda) = 1 + \frac{A_1\lambda^2}{\lambda^2 - A_2^2}, \tag{2.3}$$

where A_1 and A_1 are the Sellmeier's coefficients. The dispersion of the extinction coefficient is described by the following exponential dependence:

$$k = B_1 exp(B_2/\lambda), \tag{2.4}$$

where B_1 and B_2 are dispersion coefficients.

From the measured curve, as seen in Figure 2.4 from [11], it can be seen that with

the magnification of the thickness of the layer the refractive index grows as well. This magnification stops for the thickness $d > 110$ nm. It can be said that the coating film refractive index is close to that of the bulk.

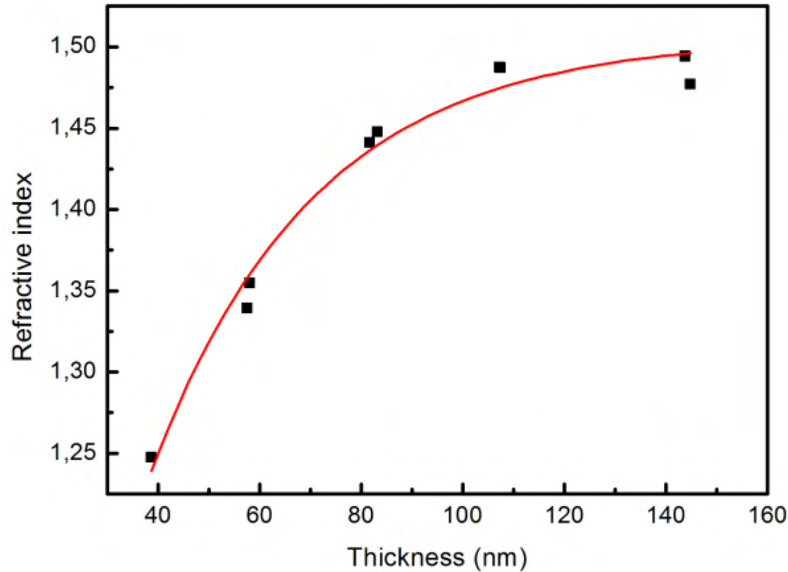

Figure 2.4: The dependence of the refractive index on the thickness of thin spin-coated PMMA films at a wavelength of 600 nm [11].

2.4 Defects in resist layers

Any parts of the film where the homogeneity of the layer is disturbed are called defects. These disturbances make the area unpredictable, which leads to faulty results. Defects that can occur during the resist layer preparation can be divided in two groups.

The first group is caused by impurities that land on the resist layer, such as dust particles and fibers. Particles and fibers can be reduced, which reduces the defects, by using a laminar flow box that filters the air that surrounds the specimen or lowers the number of particles in a whole. Air cleanliness in clean rooms is classified by the International Organization for Standardization (ISO), shown in Table 2.1 [12]. Another way for particles to get to the specimen is through the impurity of the substrate or resist. In practice, to get rid of these impurities, dust-free gases are used, as N_2. With a help of a blow gun, the surface of a substrate is cleaned immediately before deposition of the resist. Another technique used utilizes ultra-filters that are installed on the injection, before the deposition of the resists solution.

If any impurity falls on the surface of the wafer during spin coating, it makes a thickness difference in the resist that is being distributed from the center to the edge of the wafer. This defect is visible as a "comet" shape as can be seen in Figure 2.5a.

Other impurities are small resist flakes that stick to the layer and get permanently attached to the surface due to the baking (Figure 2.5b).

The other group of defects is caused by errors in the processing technology. Defects that occur during the spin coating procedure are generally observed radially. One of

Table 2.1: Airborne particulate cleanliness classes for cleanrooms standardized by ISO [12]

	≥0.1 µm	≥0.2 µm	≥0.3 µm	≥0.5 µm	≥1.0 µm	≥5.0 µm
ISO Class 1	10	2				
ISO Class 2	100	24	10	4		
ISO Class 3	1000	237	102	35	8	
ISO Class 4	10000	2370	1020	352	83	
ISO Class 5	100000	23700	10200	3520	832	
ISO Class 6	1000000	237000	102000	35200	8320	29

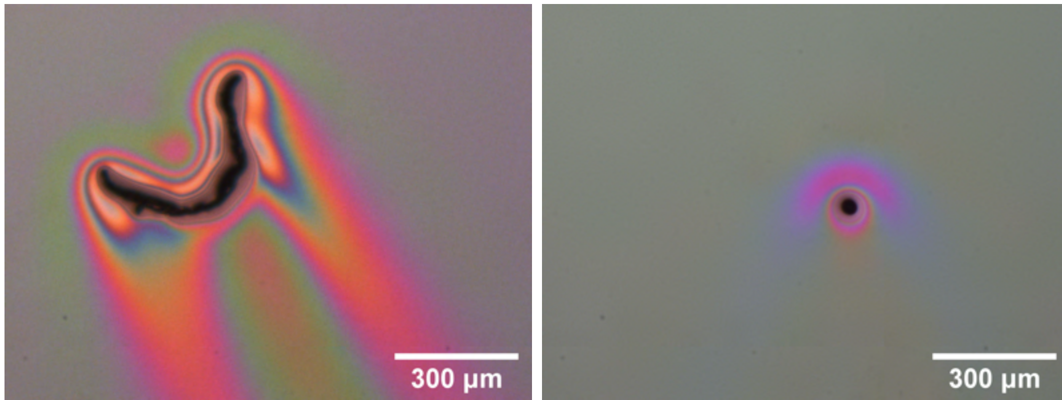

(a) A defect caused by a fiber (b) A defect caused by a resist flake

Figure 2.5: The Fiber defect appeared in the resist during the process of spin coating. The resist flake appeared in the resist during the process soft-baking.

the defects that can be detected is due to bubbles in the resist mixture. This defect can take place in the resist if air bubbles are incorporated by moving the resist in whatever manner, e.g. pipetting, transporting, shaking, etc. Defects caused by these bubbles make small spots in the resist layer with a thickness difference, which causes problems during the exposure, such as cracks in the resist layer around these spots. These defects are shown in Figure 2.6.

The chance of this happening can be lowered by slowly pouring and ultra-filtering the resist while pipetting it, degassing the mixture in a desiccator, and reducing the movement of the resist container.

Two more defects can arise. One of them is represented by spots that are not covered by any resist. This happens if an insufficient amount of resist is applied. Spots will appear on the edges of the substrate due to the principle of the already mentioned spin coating process.

The other of the two is caused due to an insufficient centering of the wafer on the spin coater. Microscopes are not able to see this defect that easily due to a small field of view. As can be observed from Figure 2.3, this defect is more easily observed at the macroscopic scale, by the naked eye or optical instruments which have a larger field of view than a microscope.

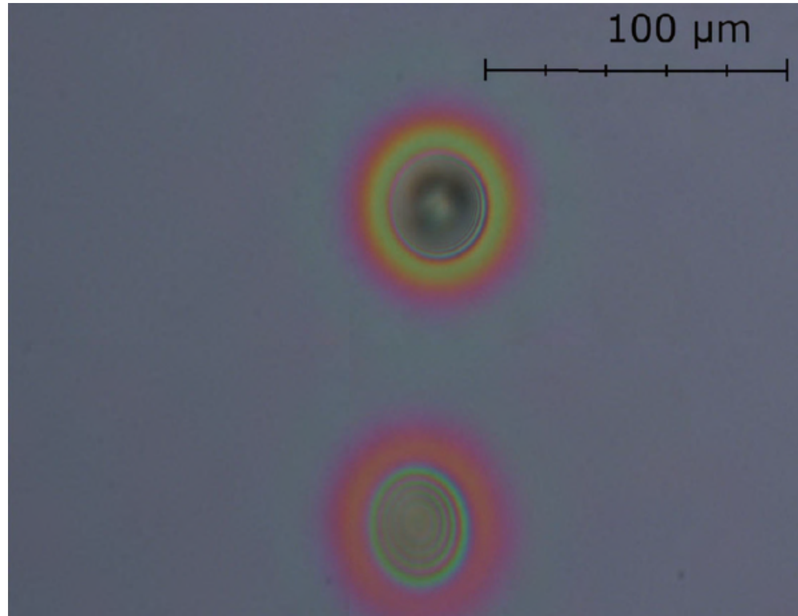

Figure 2.6: Defects caused by micro bubbles [2]

2.5 Inspection of resist layers

This chapter discusses the types of microscopy used in electron lithography. Their basic principle is discussed and what effect each type has on the undeveloped resist layer when used.

2.5.1 The Scanning Electron Microscopy

The Scanning Electron Microscopes (SEM) are very often used to observe structures created using EBL. For the SEM to work, needs the observed sample to be conductive, which resists and search defects are not. Furthermore, another distinct disadvantage is that the electrons would expose the layer, which is undesirable. To make matters even worse, the SEM needs to work in a vacuum, which adds to the cost and adds the requirements for the setup. [13][14]

All of the above concerns make this technology not usable for resist layer inspection. [15]

2.5.2 The Atomic Force Microscopy

With the Atomic Force Microscopy (AFM), only the topography of the sample can be obtained. Therefore, inspection of any defects that may be observed in the resist is not possible. At the same time, it is not possible to decide whether the inequality found is in the resist or an external material [16]. The AFM lacks the speed as the typical speed of a tip is around $30\,\mu\mathrm{m\,s^{-1}}$. To get the perspective, the scanning of a $100\,\mu\mathrm{m} \times 100\,\mu\mathrm{m}$ area by $1024\,\mathrm{px} \times 1024\,\mathrm{px}$ takes around 1 hour. [17]

As a result of these inadequacies, the AFM is not an adequate method for the inspection of resist layers.

2.5.3 The Visible Light Microscopy

The Visible Light Microscopy (VLM) uses light with a wavelength in the range of 400–700. It was found that with a help of the the VLM it is possible to get a resolution as good as half of the wavelength of the microscopes illumination source. That means, at best, that the attainable resolution is 200 nm. [18]

When it comes to the usage of VLM in inspection, it overcomes all the disadvantages of the other methods that have been mentioned. The VLM, in comparison with SEM, does not expose the resist and works in any transparent atmosphere. VLM is not limited by properties of materials. The transparent particles can be seen thanks to the Frits Zernikes technique in which the phase contrast illumination is used [19], for which Mr. Frits received the Nobel Prize in Physics in 1953 [20].

3. Measurements and results

As a result of this bachelor thesis, a system called WaferScan in Figure 3.1 and its controlling software were created. The system is designed to take images of the wafer in a user-chosen zone by moving the wafer and then process the acquired images in a way that it founds all the defects that are captured. The process of completion of the whole system is described in two subsequent sections, 3.1 and 3.2.

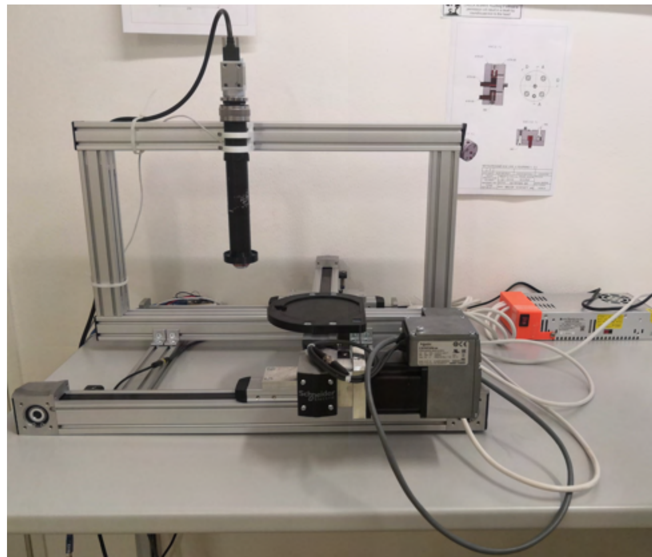

Figure 3.1: WaferScan, a measuring system

3.1 Hardware design

This section describes each mechanical and electronic part that makes up the system. Moreover, it gives a reader a simple overview of connections that are necessary for energy and informational transport.

3.1.1 Mechanical parts

The movement of the system is driven by two 3-phase stepper motors from Schneider electric company. Each motor controls only one assigned axis. The torque of each motor is transmitted to a toothed belt which then relocates the holder of the wafer on the corresponding axis. Each step of the motor corresponds to 4.18 µm.

Two designs of wafer holders were created to hold different sizes of the wafer, a 4-inch, and a 6-inch ones. A model of the 4-inch holder is displayed in Figure 3.2. To change between them, all screws need to be removed. These holders were created by a Prusa's 3D printer and are designed in such a way that the wafer has no space to be moved by a movement of the belts. To remove a wafer, a small gap was implemented into the model for user access. On the opposite side of the holder, there is a space for the facet of the wafer and the calibration cross. The cross was printed on a resin 3D printer because of the high precision requirements and then inserted into the holder.

All aluminum profiles were bought from the company Item. Profiles have rails that allowed an easy modulation during the development of the system. They hold all components together to make the system stable and coherent.

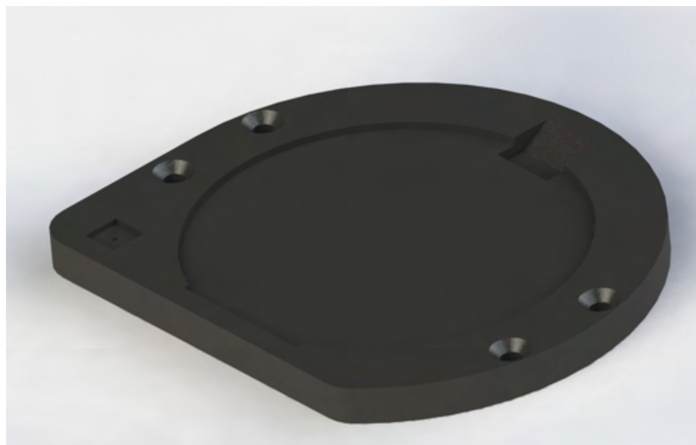

Figure 3.2: A model of a 4-inch wafer holder created in *Solidworks 2020*

3.1.2 Electronics

Figure 3.3 shows the main electrical components of the system.

Both already mentioned stepper motors share the power supply that provides 36 VDC. Axes are equipped on each end with an inductive proximity sensor. These sensors activate when the holder of a wafer gets near. If sensors activate, the power to the corresponding axis stepper motor is turned off to prevent any further damage that could occur.

Another electronic component around which more electronics are situated is a LED ring consisting of 16 diodes. The ring is connected to the Arduino UNO which can work as a communication canal and a power supply. In the system setup, Arduino works only as a communication canal due to its limitations. Arduino is able to provide only 500 mA which is not enough to achieve the maximum illumination that the LED ring is capable of. For maximum capabilities, 800 mA from the external power source is provided.

The camera's power demand is only 4,4 watts. Such a demand is satisfied with a USB 3.0 connection.

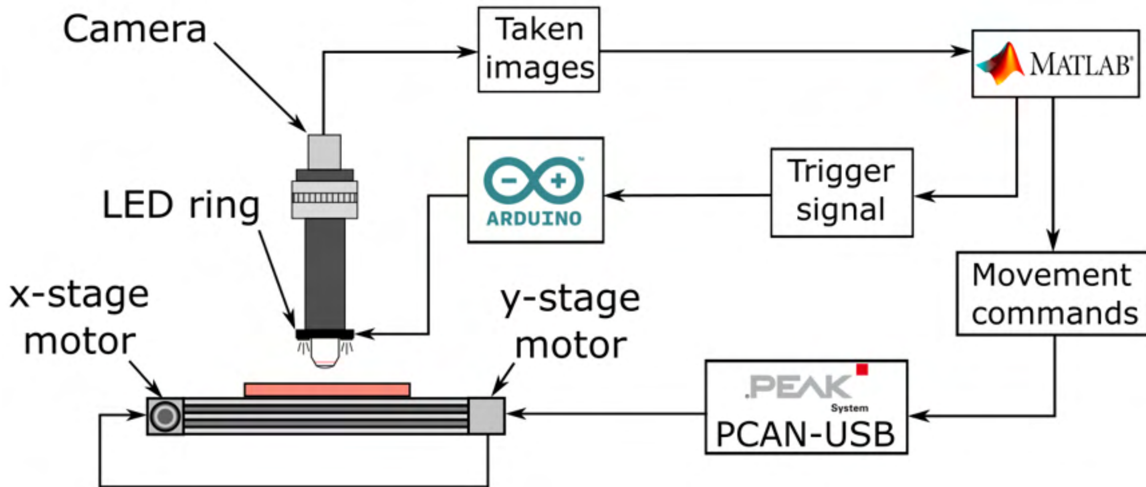

Figure 3.3: A chart of electronic devices and communication canals

3.1.3 Optics

In the search for the optimal optics, we looked for certain parameters that would lead to the best possible results. One of these parameters was the resolution of the chip. With higher resolution the advantage comes that the system does not have to take as many images, which speeds up the analysis process. Another important parameter was the type of shutter of the camera. Cameras are usually equipped with a rolling shutter, but this would introduce errors into the system due to the rolling shutter effect. To avoid this error, we looked for a camera that has a global shutter. This type of camera captures data from the chip at a single point in time, outperforming other shutter types. For the device to have more features in the future, there was also a requirement that the camera should be able to capture color images.

The chosen camera that fits all these parameters is a Basler s2A 4504–18ucPRO. The camera is equipped with a color square shaped CMOS chip that measures 12.3 mm × 12.3 mm and has a resolution of 4504 pix × 4504 pix which corresponds to 20.2 Mpix. The version type "PRO" comes with more accessories to control the settings of the camera. One of these accessories is the function "Compression Beyond". This function allows compressing the size of an acquired image from the camera to a size < 1 MB.

The optical setup of the camera consists of an objective lens, a tube lens, and an extender. The objective lens has a 18.5 mm working distance from the sample, a 4× magnification, and a numeric aperture $NA = 0{,}1$. From an objective lens, a collimated light beam goes to the tube lens that has 180 mm focal length and focuses a beam of light onto the chip. In between these two, an extender with a focal length extension of 1,5× was later added to get full coverage of the chip by a beam and to achieve a bigger magnification.

The magnification the system achieves is computed by multiplying the magnification of every component of the optical setup. This setup magnifies the image 6×. The angular resolution can be calculated by an equation [21]

$$R = \frac{0.61\lambda}{NA_{sys}}, \tag{3.1}$$

where NA_{sys} is a numerical aperture calculated as $NA/1{,}5$ and λ is a wavelength of the observed radiation. In the calculation, the value of lambda was chosen to be a green color $\lambda = 546.07\,\text{nm}$. This value corresponds to the Fraunhofer's line "e". After the substitution and calculation, the angular resolution, in theory, is at its best $R = 6.66\,\mu\text{m}$.

For the control, if the theory corresponds with practice, the setup was tested on the standard. The standard had a 10µm and a 5µm grid. The photographs of the grids captured by the camera and the described optics are shown in Figure 3.4. The optical setup can distinguish individual lines from each other in the case of 10µm. In the case of the 5µm grid, the lines are indistinguishable from each other.

The field of view of the optics was also measured on the standard. Using ImageJ software image analysis, the field of view of the optics was calculated to be 2277µm.

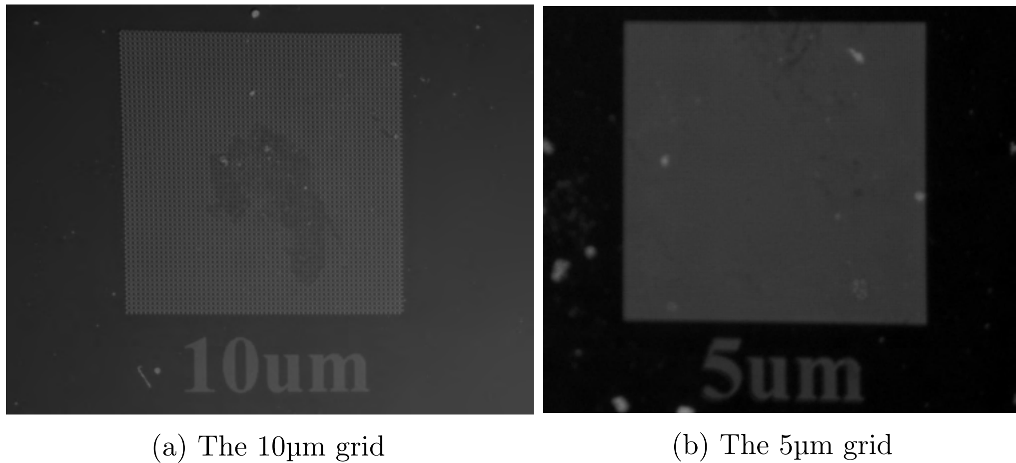

(a) The 10µm grid (b) The 5µm grid

Figure 3.4: Cropped images of the standard captured by the optical setup of the WaferScan

When observing the standard, it was also possible to see what aberration the system is most burdened with. The system is heavily loaded with barrel distortion. This can be observed very clearly in Figure 3.5, mostly in the corners, where lines that should be straight curve and therefore distort not only their positions but also their sizes.

The illumination of the observed sample is solved using a LED ring. The ring is mounted in a 3D printed holder which, thanks to a designed small clearance, fits around the objective lens. In this way, a type of illumination is achieved which is called lateral illumination. With this type of illumination, the disadvantage comes that only opaque defects can be observed. This limits the use of the WaferScan only to two types of defects, namely dust, and fibers. These defects are then shown as white spots in the images.

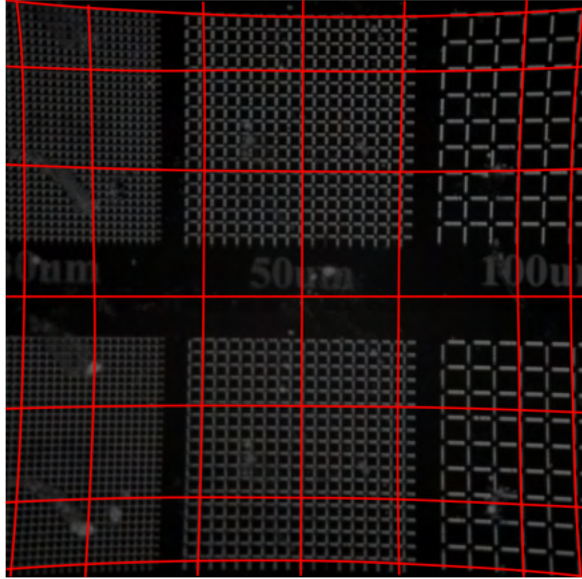

Figure 3.5: A visualization of distortion of the optical setup

3.2 Algorithmization

This section describes the options of the system that are provided to the user and gives the reader a step-by-step understanding of how the Main function that looks for the defects on the wafer works and what data the user gets from performing it. In Figure 3.6, it can be seen that the process is divided into three steps, “Initial Process”, “Scanning Process”, and “Image Processing”. These steps are so important that they are split into separate subsections.

For the most part, the official MathWorks© support site was used as a source of information for development.

3.2.1 Communication

All information that is communicated in the system comes in touch with a computer. The computer acts as the start or endpoint of all channels. It has 3 USB cables plugged in to fully function with the system (Fig. 3.6).

First, the USB communicates with stepper motors. Stepper motors are designed in such a way that they can communicate only by way of the Controller Area Network (CAN). Devices connected to CAN send information in frames. A CAN frame consists of the segments that are shown in Figure 3.7. The CAN frame carries data about arbitration ID, data bytes, acknowledge bit, etc. [22]

The computer only needs to work with the “Data field” part of the frame and with the information at whom the message is aimed. Messages in the “Data field” look, for example, this way [43 40 48 5 44 1 0 0] (this command sets the speed of the corresponding motor to 300 rotations per minute). The first 4 bytes determine what value to change and the last 4 bytes specify to which value. This data is packed with the corresponding ID of the rotor and sent from the PC to a PCAN-USB adapter. The adapter then translates the decimal ’Data field’ to hexagonal and makes from a

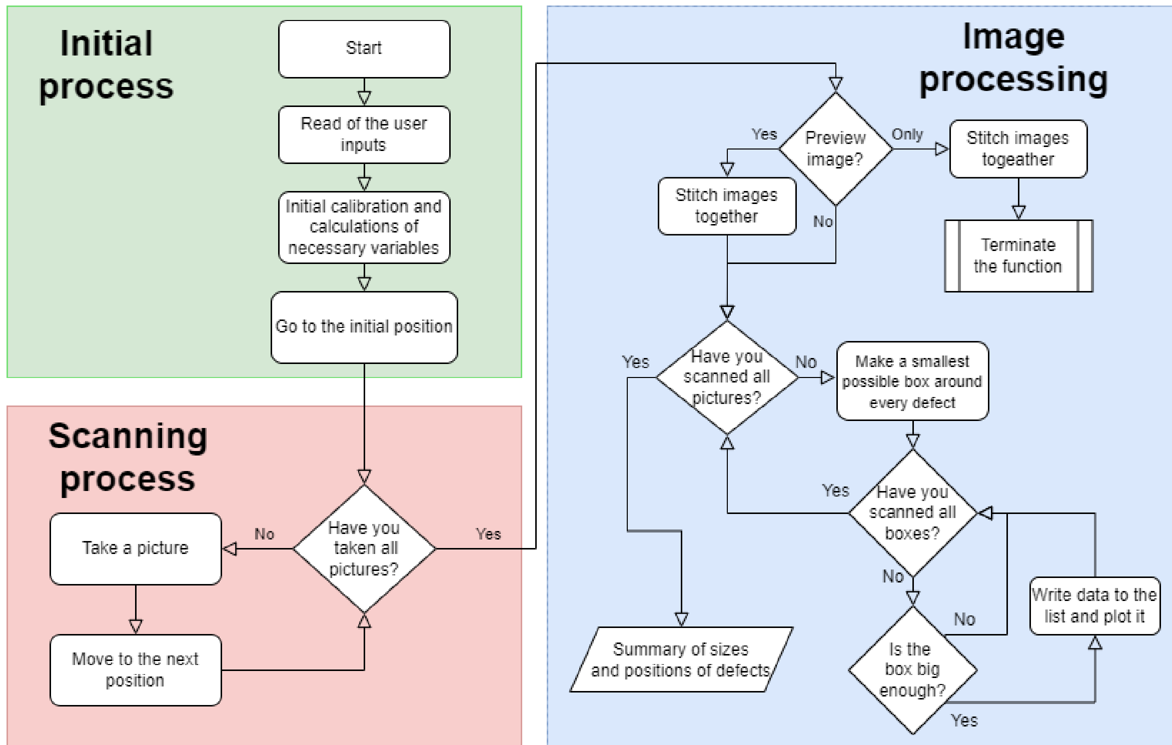

Figure 3.6: A flow chart of the Main function algorithm

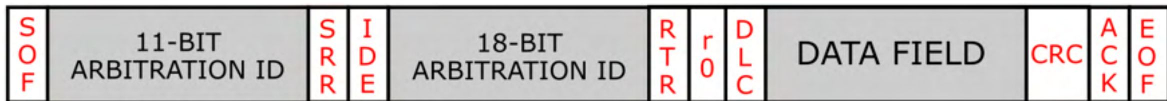

Figure 3.7: The standard CAN frame format

full packet from the received information. The message mentioned above translates to [2B 28 30 5 2C 1 0 0]. This packet travels through CAN and is executed. A Vehicle Network Toolbox must be installed into the Matlab for this to work.

The second USB communicates with Arduino. It communicates in the American Standard Code for Information Interchange in short ASCII. A program is installed within Arduino that starts the procedure when a certain symbol from ASCII comes to a PC communication pin.

The last USB communicates with the camera. For communicating with the Basler camera, another toolbox is provided from Matlab. An Image Acquisition Toolbox makes it possible to chance the properties of the camera and take a picture or a video.

3.2.2 The graphical user interface

The software's graphical user interface (GUI) is implemented by using Matlab's application GUIDE. The GUI is shown in Figure 3.8 with a description of all functions that are provided to a user in it.

(1) A plot with a wafer outline and a red square that shows the zone that the user wants to be scanned. During the Main function, the plot is zoomed into the scanned zone.

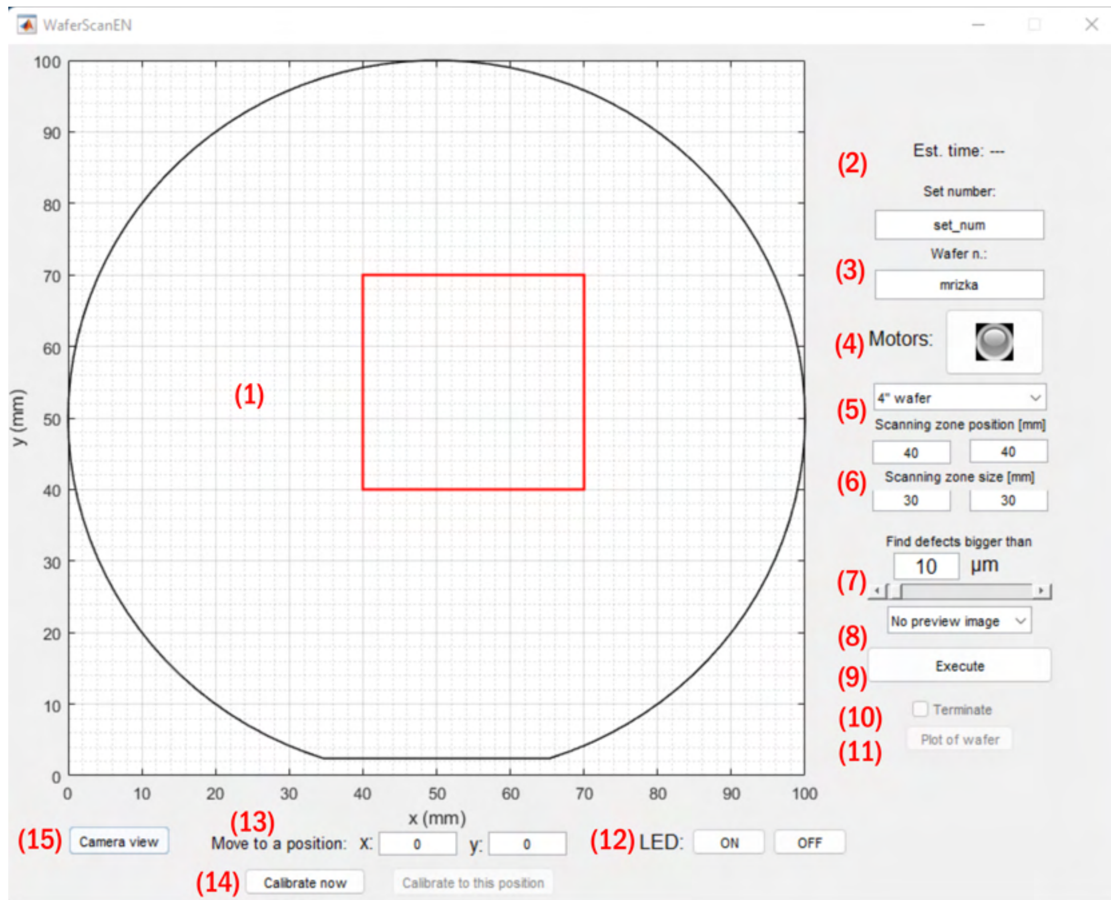

Figure 3.8: The graphical user interface of the WaferScan application

(2) An estimation of the length of the scanning process until its completion.

(3) Editable texts to name the set and number of the wafer.

(4) A power switch of motors. It allows the user to manually move the axis if necessary.

(5) A pop-up menu of the wafer size. Upon choosing the plot with a description (1), it updates itself.

(6) Editable boxes, where it is possible to adjust the position of the lower-left corner and the length of the sides of the red square displayed in the plot (1). The plot updates itself upon choosing.

(7) Here, a selection is made as to the size of the smallest defect the software should look for. The user can do this either by typing in the editable box or by using the scroll bar.

(8) A pop-up menu that determines whether the “Stitching” function is executed and, if so, how. This function is explained further in Chapter 3.2.5.

(9) The button which initiates the Main function. The whole function is described in the Chapters 3.2.3, 3.2.4, and 3.2.5.

(10) The check box that upon clicking tries to stop the Main function without any errors.

(11) After the Main function is finished, this button returns the user to the preview in the plot (1) so that the user can see the defects in relation to the wafer.

(12) Buttons to switch the LED ring on and off.

(13) Editable boxes that move the wafer so that the camera faces the inscribed position.

(14) The "Calibrate now" moves the wafer in a way that the calibration cross, mentioned in Chapter 3.1.1, is situated under the camera, opens the view of the camera, and switches the LED ring on. If the cross is not in the middle of the view, the user can adjust the position using the editable boxes (13). When the user is done adjusting, the button "Calibrate to this position" needs to be pressed to proceed. The coordinate system is thus repositioned to match the new camera position which may move slightly over time.

(15) This button pops a new window in which the view of the camera is shown.

3.2.3 Initial process

This process takes effect right after the trigger of an Execute button.

First of all, the calibration process starts. That is done by setting one corner of an aperture as the beginning of the coordinate system. Motors then move the wafer holder towards that corner. The activation of the inductive proximity sensors indicates that the wafer holder has reached the beginning. When this procedure finishes, the system sets boundaries for the movement to prevent errors that occurred when being tested.

After the completion of calibration, the calculation of how many pictures need to be taken begins as well as the calculation of the starting position of the system, and the movement parameters. The system then sends a signal "255" to Arduino. This signal corresponds to a process that sets the LED ring at full power. The final step is to move the wafer holder to the calculated beginning position. This position is designed in a way that the lower-left corner of the scanning zone is in the lower-left corner of the first taken picture.

3.2.4 Scanning process

The target of this process is to take images of a whole user-desired zone. All of the calculations were made in the Initial process 3.2.3. The scanning process is described in Figure 3.9.

At each step of the camera, one image is acquired. The raster scans along the "zig–zag" trajectory that is displayed by a blue line. The red square is the user-desired zone

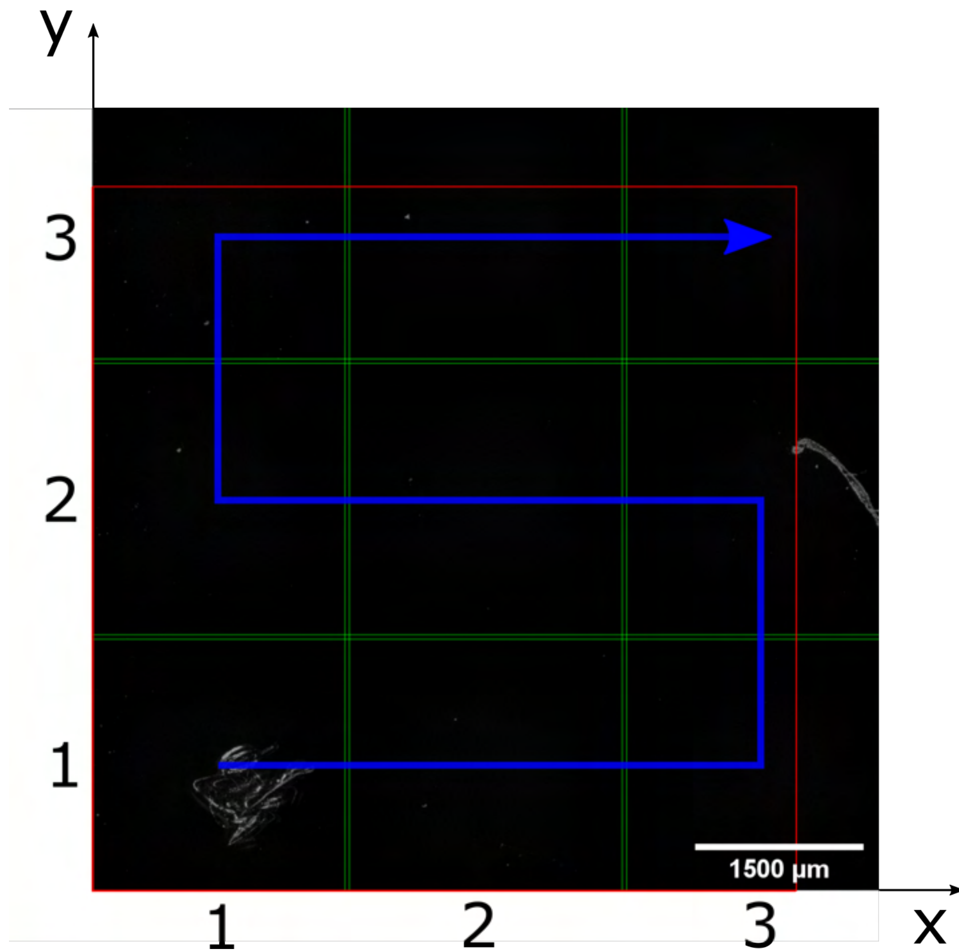

Figure 3.9: The blue line is the “zig-zag” trajectory, the red square is the user-desired zone and the green lines show the overlap of the images

that is being scanned. In this image, the zone is set to 6.5 µm. Every image overlaps the adjusting ones and is set to overlap by 20 µm. For presentation purposes, Figure 3.9 has the overlap length set to 100 µm m and can be seen as a gap between two green lines that run next to each other. This is done to prevent any defect to be overlooked.

Each taken image is saved into the “Temp” folder. This folder holds every acquired image and each name of the image contains the information about the place the image was taken. It is saved by the position on the axis in the format “y_x”.

3.2.5 Image processing

During this part of the procedure, images are post-processed to get the data from them.

The first part of the process is the stitching function. This function gives the user an option to create one whole image from partially acquired images. The stitching function works as follows. Images that share the same y-value are loaded as matrices and stacked one after the other to form one complete matrix. This matrix then represents one complete series of photographs taken. This is done with all rows of images. These matrices are then “stitched” into one whole matrix and exported as another image. Such an image is represented by the Figure 3.9.

Users have the option to choose from three options. The first option is to not create the image and continue with analyzing the image for the defects. The second option is to create the stitched image and continue with the first option. The third option gives the user the ability to create only the stitched image. This function is used mostly for testing. It allows the user to examine the samples that already have some fully developed patterns. The third option then executes the algorithm utilizing a function called "Terminate".

After the preview, the image analysis follows where the defects are looked for.

The whole process is done in cycles by loading and evaluating the images one by one. The images that are captured by the system do not contain much noise or parasitic light. As a result, there is no need for the image to undergo its removal where the size of the defects could then be distorted. The only image modification that the system does is the conversion from a grayscale image to a binary image. This is achieved by thresholding.

In the system, the thresholding is a constant t. The process is defined by the following equation, where x represents the pixel value in the grayscale image:

$$
\begin{aligned}
x \geq t &\Rightarrow \text{the new pixel is equal to 1} \\
x < t &\Rightarrow \text{the new pixel is equal to 1}
\end{aligned} \tag{3.2}
$$

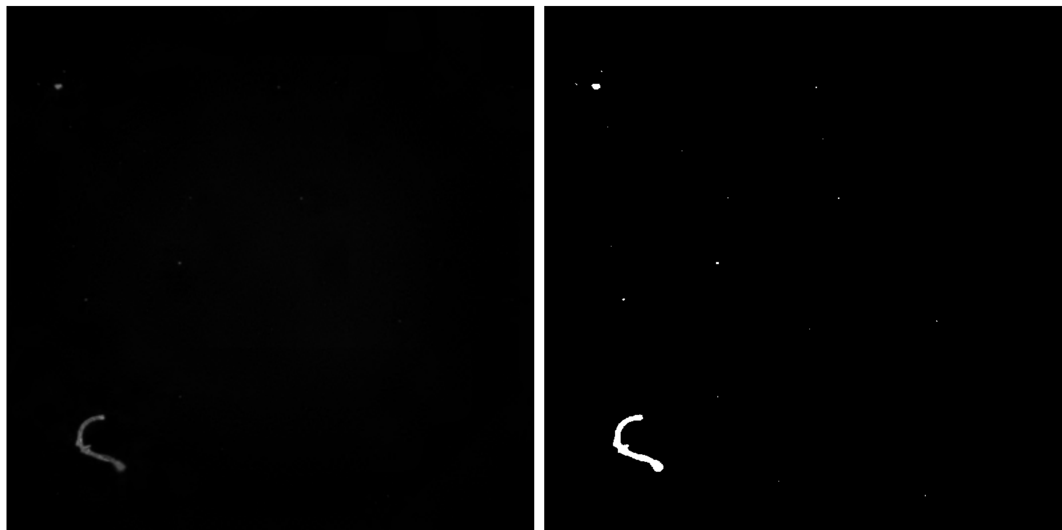

(a) Unmodified image (b) Thresholded image

Figure 3.10: The image before and after the thresholding

In the system, the thresholding value is set to be constantly 20. After this conversion, the pixels corresponding to value 1 are taken as defects, and pixels with value 0 are taken as a background.

The next step is to measure the properties of defects in the image. For this purpose, a region props function of Matlab Image Processing Toolbox was used, with a property "Bounding Box". It looks for the smallest box containing the whole defect. It then

returns the coordinates of the upper-left corner of the box and the lengths of its sides. If we know the dimensions of the field of view and the image resolution, the obvious step is to convert the measured values in pixels to micrometers.

The system then goes through the list of boxes that now represent the defects. If any of the sides of the box are larger than the value specified by the user (done in GUI 3.2.2 function (7)), this defect is written to the final list of found defects and further examined by artificial intelligence to determine whether it is dust or fiber.

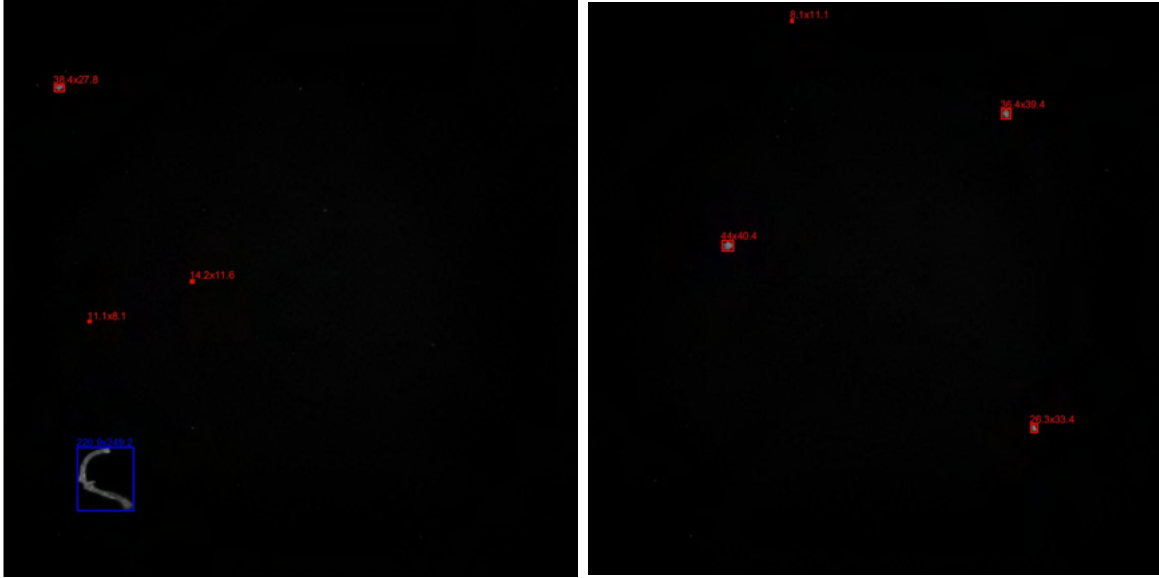

(a) An image with a fiber and dust particles (b) An image only with dust particles

Figure 3.11: Measurement of the size, position, and type of the defects; red boxes surround dust particles and blue boxes surround fibers

The examination is done using a function "corr2". It computes the two-dimensional correlation coefficient between two matrices. The algorithm itself computes the correlation coefficient r using

$$r = \frac{\sum_m \sum_n (A_{mn} - \bar{A})(B_{mn} - \bar{B})}{\sqrt{(\sum_m \sum_n (A_{mn} - \bar{A})^2)(\sum_m \sum_n (B_{mn} - \bar{B})^2)}}, \tag{3.3}$$

where A is the matrix corresponding to the defect, B is the matrix representing the image of dust or fiber with which the A is compared, $\bar{A}$ is the average of matrix A elements, and $\bar{B}$ is the average of matrix B elements.

The compared images B are displayed in Figure 3.12.

Depending on which comparison shows a higher correlation value, it is decided whether the defect found is a dust particle or a fiber. This information is then written to the final list to the corresponding defect.

As a result of this process, the user is provided with a visualization of where each defect is located and an Excel file where the position, size, and type of all the found defects are saved. The types of defects are distinguished in the visual representation by their colors, with red corresponding to dust particles and blue to fibers (Figure 3.11). [28]

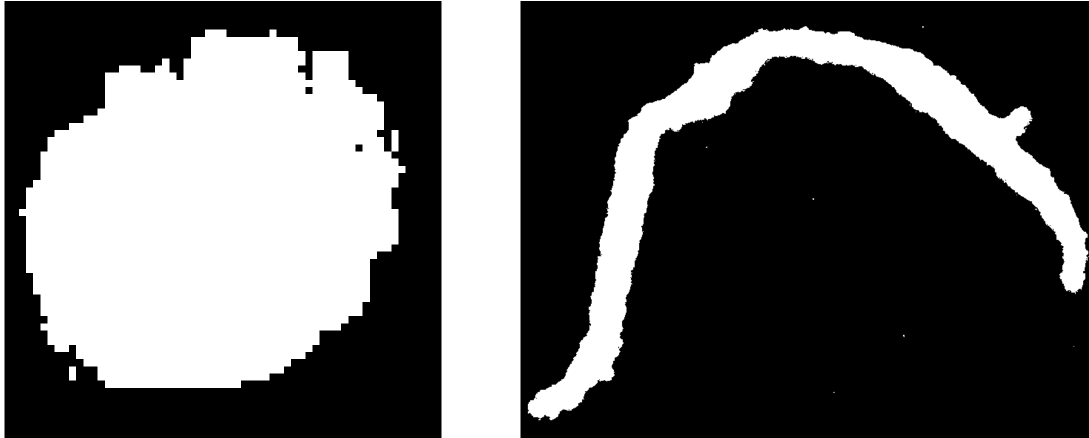

(a) An image representing the dust particle (b) An image representing the fiber

Figure 3.12: Images that are used for a correlation function “corr2”

3.3 Measurements

This chapter focuses on the measurements that were taken to verify the capabilities of the developed WaferScan. This involves looking for bugs in the system and also testing the limits that the system might encounter when used on better than test samples. The artificial intelligence that looks for the type of defects was turned on only in the measurement in Section 3.3.3.

3.3.1 Comparison of the manual method with software

For the first measurement, two wafers were prepared. The preparation of the resist layers took place in the Institute of Scientific Instrument's clean rooms. A measurement of the number of particles in the room was made (Figure 3.13), indicating that clean rooms fall into the ISO Class 6. The concentration of PMMA in the solution was 9 %. The spin-coater spin speed was set to 3000 min^{-1} and the duration of the process to 1 min. The spin-coater was put in the flow box, however, it was forgotten to be turned on during the spin-coating procedure. This led to more defects on both wafers. The soft-baking procedure was set to 150 °C, the duration to 9 min. Unlike the spin coating, the soft-baking took place in the flow box that was turned on.

The first measurement's goal is to compare the precision of the currently used manual method by Mr. Král against the constructed system. Moreover, it was a test of how long it would take for the system to analyze a 50 mm × 50 mm area for 10 µm defects. Both measurements were made in the flow box.

The wafer number 1 was set to be analyzed first by Mr. Král. His analysis took around 1 hour and was able to find 9 defects in the agreed area. The outcome data set is shown in Figure 3.14a. Immediately after that, the analysis by the WaferScan system took place. The full procedure took 27 mins and found 33 defects. The outcome data set is shown in Figure 3.14b.

The second wafer was prepared for testing first by WaferScan and then by Mr. Král. The software found about 60 defects and took 50 mins. The analysis took so long due

Figure 3.13: Results of the measurement of the number of particles in the room

to the lack of RAM. Manual analysis was not carried out because of the number of faults that were found by the AI. The manual method would take around two hours with this number of defects.

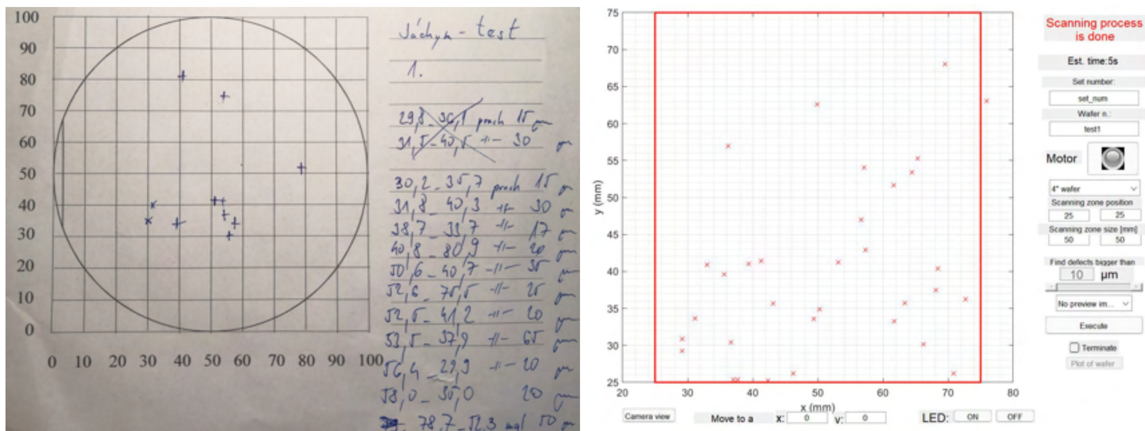

(a) Manually analyzed data set

(b) Data set of the WaferScan

Figure 3.14: Results of the first measurement

The conclusion of this experiment is as follows. The system has the potential to achieve greater defect measurement accuracy than the current manual method. Another discovery is that the defects found by WaferScan have not corresponded exactly to the positions found by the manual method. As a result of the discovered error, calibration of the system was done more precisely.

The calibration means a process in which the constants that say how large the field of view of the camera is and what distance one stepper motor corresponds to had to be measured once again, as the movement and all calculations of the positions are based on these constants.

3.3.2 Consistency and efficiency

In this measurement, a set of consecutive scans was performed. Scans were done on a previously measured wafer number one in a 40 mm × 40 mm area. The smallest size of the defects that were looked for was set to 15 µm to reduce the duration of scanning.

The WaferScan was equipped with a wafer holder that had no calibration mark and with a small clearance between the wafer and the holder.

This measurement aimed to check whether the system introduces any defects into the sample. If the result of this measurement had failed to be positive, the device would not find any effective use in real practice. Another parameter that was monitored is whether the axes move consistently. This was measured by selecting some defects and observing whether the positions of these defects changed in any way over the course of all measurements.

The measurement of the number of particles found by the WaferScan is shown in Figure 3.15. From these measurements, 2 defects were selected and their data are in Table 3.1. In the table, x and y tell the position of the defect on the wafer, and the dx and dy define the size of the defects.

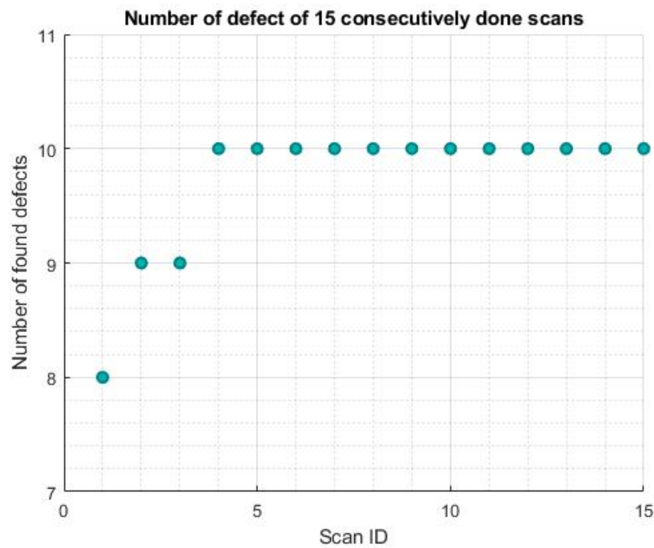

Figure 3.15: The number of found defects in 15 consecutive scans

The graph in Figure 3.15 shows that the number of faults detected by the system has increased slightly since the beginning and has not changed since the 4th measurement. After the initial defect detection, the system found defects in each subsequent measurement. This indicates that the measurement by the system is consistent.

From Table 3.1, the accuracy of the system can be measured. Due to this a row "Manually" has been added to the table to define the position of the defect measured manually by the metallograph.

The differences in the comparison of the sizes of the defects are not that significant. The biggest difference is in the dy size of the first defect. The error can come both from the error of the constant that tells the size of the pixel and from the human error.

Every scanning cycle took around 16 mins.

When comparing the manually and software measured values of the position of the first defect, the deviation of the defect position on the y-axis is in the order of tenths of a millimeter. For the x-axis, the result of the comparison is not that optimistic. The difference between these measurements is in the order of a millimeter, which is a significant deviation. This error indicates that the constants for the x-axis that define

Table 3.1: Tracking of two defects in 15 consecutive scans

	First defect				**Second defect**			
Scan ID	**x/mm**	**y/mm**	**dx/μm**	**dy/μm**	**x/mm**	**y/mm**	**dx/μm**	**dy/μm**
1	32.6	73.2	48	54	59	48.5	110	124
2	32.8	73	48	54	59	48.5	112	128
3	32.9	73	47	53	59	48.6	111	128
4	33	72.9	45	52	58.9	48.6	111	129
5	33	72.8	46	53	58.9	48.6	108	126
6	33	72.9	46	52	59	48.6	109	127
7	33	72.9	46	52	58.9	48.6	111	129
8	33	72.9	47	52	58.9	48.6	108	127
9	33	72.9	45	53	59	48.6	109	127
10	33	72.9	45	52	59	48.6	110	128
11	33	72.8	47	53	59	48.6	108	126
12	33	72.9	46	53	58.9	48.6	108	127
13	33	72.9	46	52	58.9	48.6	107	126
14	33	72.9	46	52	59	48.6	110	129
15	33	72.9	46	52	59	48.6	108	126
Mean	33.0	72.9	46.3	52.6	59.0	48.6	109.3	127.13
Dispersion	0.07	0.06	0.8	0.7	0.05	0.02	1.3	1.1
Manually	30.9	72.7	43	46	59.0	47.6	108.5	125.5

the movement of the axis or the position of the origin of the coordinate system might be set wrong. For the second defect, the comparison results are almost identical, the difference is that for the x-axis position, the results are nearly identical and for the y-axis, the difference in positions is significant. The results of the comparison are opposite to the first defect.

As a result, tracking of the third defect was performed. The measured data are in Table 3.2 from which a difference of both axes was in the order of millimeters. The defects are displayed in Figure 3.16. Red marks are data from the software method and the blue marks are the manual measurements.

Due to the inconsistency of the error, the cause cannot be the faulty measured constants that were mentioned. In the Table 3.1, for the first 4 measurements the positions of the defects change, after that, the position is almost constant. The wafer is placed in the holder with a large clearance of several millimeters. When the motors move the axes, the speed increases by leaps and bounds, resulting in small but significant movements for the measurement. This may be the cause of the error. The measurements, therefore, led to the creation of a new, and more precise, holder.

3.3.3 Improvement of the measurement

This measurement was performed with a new wafer holder, where the clearance was minimized, and a calibration mark. During the setup update, a calculation error was also found which, in the worst case, introduced an error equal to the size of the field of view into the position of the defect in the final data. Moreover, in this measurement,

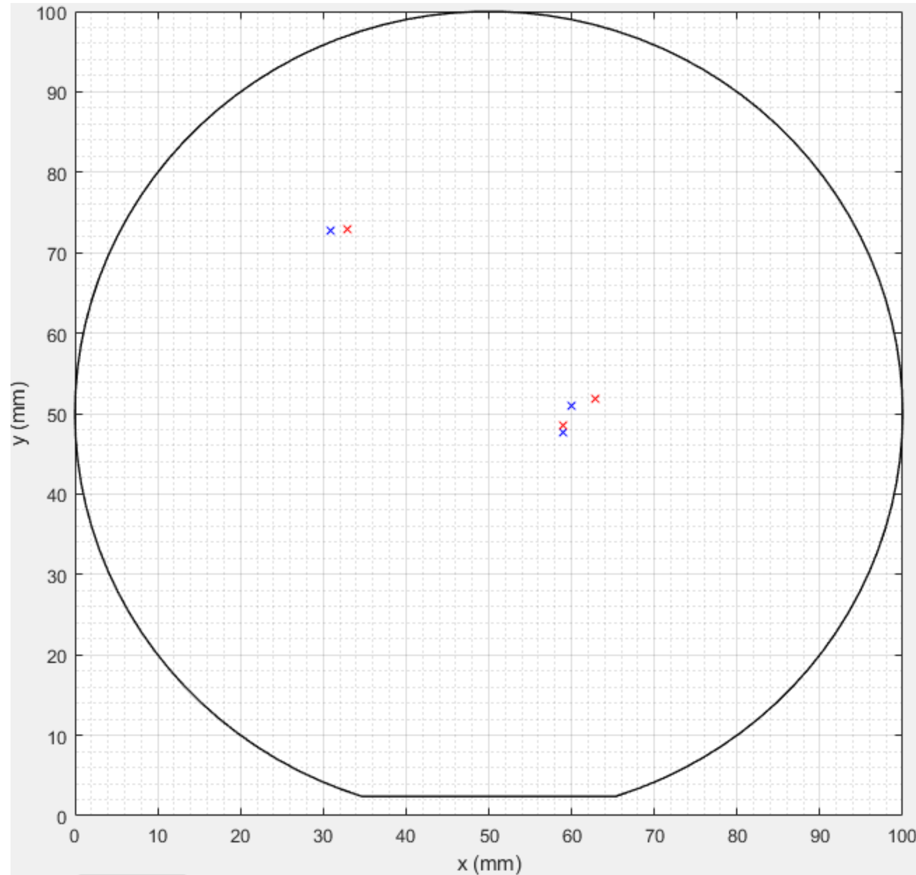

Figure 3.16: Three defects detected by the software (red crosses) and by hand (blue crosses)

an AI was finally enabled.

Because of these errors that affected the previous measurements, this measurement has all parameters set the same. The only difference is that the measurements were performed 5 times and not 15 times. The same wafer as the previous one was used, so that at least one defect could be tracked that was detected last time and to compare to what extent the improved system yields better measurements.

As a result of this measurement, the Table 3.2 with one tracked defect was created.

From the table, it is easy to see that the positions found by the upgraded setup correspond more with actual positions of the defects. Moreover, the positions of the defects no longer shift over the course of several consecutive measurements, which is most likely a result of the more precisely formed wafer holder.

In between these measurements, there was a significant time difference. In the previous measurement, the scanning took 16 mins. In this measurement, the scanning took 24 mins. This time difference is most likely due to the implementation of artificial intelligence that decides the type of defect, as other parameters remained as they were in the previous measurement.

Table 3.2: Tracking of two defects before and after the upgrade of the device

	Old measurement				Upgraded measurement			
Scan ID	**x/mm**	**y/mm**	**dx/µm**	**dy/µm**	**x/mm**	**y/mm**	**dx/µm**	**dy/µm**
1	62.9	51.6	61	49	59.9	50.5	39	39
2	62.9	51.7	61	48	59.9	50.5	40	41
3	62.9	51.8	61	46	59.9	50.5	40	41
4	62.9	51.8	62	47	59.9	50.5	37	39
5	62.9	51.8	61	47	59.9	50.5	39	40
6	62.9	51.8	61	46	-	-	-	-
7	62.9	51.8	62	45	-	-	-	-
8	62.9	51.8	61	46	-	-	-	-
9	62.9	51.8	61	47	-	-	-	-
10	62.9	51.8	61	47	-	-	-	-
11	62.9	51.8	60	46	-	-	-	-
12	62.9	51.8	61	46	-	-	-	-
13	62.9	51.8	61	46	-	-	-	-
14	62.9	51.8	61	45	-	-	-	-
15	62.9	51.8	61	45	-	-	-	-
Mean	62.9	51.78	61.1	46.4	59.9	50.5	39	40
Dispersion	0	0.03	0.3	0.9	0	0	0.8	0.8
Manually	60	50.9	43	44	60	50.9	43	44

3.3.4 The effect of ambient light on the measurement

This measurement aimed to see if the lighting in the room had any effect on the measurement.

This measurement was carried out as follows. A measurement was taken of the polymer layer under normal laboratory conditions and then another measurement was taken with the entire assembly covered to limit ambient light in this way. This measurement was then repeated for the standard to also see if the lighting had any effect.

For the measurement of the polymer layer on the wafer, the results were the same. The ambient light did not affect the final data.

The measurements of the standards were performed by taking a picture of a zone that corresponded to 4 images × 4 images, and these pictures were then stitched together by the function “Stitching”. These stitched images were then processed by a function “corr2” from which the correlation value was calculated to be 98 %. As you can see in Figure 3.17, the measured standard shifted slightly during the process of covering the WaferScan. This shift also affects the correlation result.

(a) The sample exposed to ambient lighting (b) The covered sample

Figure 3.17: Correlated images taken with and without ambient lighting

4. Conclusions

This thesis aimed to create a system capable of detecting defects in thin polymer layers fully automatically. This development included both hardware and software solutions to the given problem.

In the first part of this work, literary research of the EBL process was done. It covered the optical, mechanical, and chemical properties of EBL, the preparation of the resist layer, and the types of inspections that are used on wafers, where it was discussed whether their use would be effective on unexposed layers of resist. Defects which may occur in the resist were divided in two groups – defects caused by impurities and defects caused by the processing technology of spin coating and soft-baking.

The first step in developing the system was to create the hardware. The movement of the wafer was solved by two precise stepper motors that transmit their torque using a toothed belt. A special 3D printed wafer holder was then attached to these toothed belts. The holder was designed so that the wafer would fit into it with minimal clearance and further so that a calibration cross could be accurately formed into it. This cross was also printed on a 3D printer, but resin was used here instead of plastic.

Next, a Basler s2A 4504–18ucPRO camera was selected and purchased as the optimal camera for this facility. An optical setup was then designed and subsequently assembled for this camera, which consisted of an objective lens, a tube lens, and an extender. This optical setup achieved a distinguishability of sub 10 µm and a field of view of 2277 µm. This entire setup was then mounted over the area where the sample was moved by motors. Side illumination of the sample was provided by a LED ring, for which a holder was re-printed on a 3D printer from plastic to wrap around the lens. The ring was controlled by the Arduino. The computer was then connected to the Arduino, the motors, and the camera.

The hardware development was followed by software development. The development of the custom software was done in Matlab with the GUIDE, which creates the graphical user interface, and two additional extensions called Image Acquisition Toolbox and Vehicle Network Toolbox. The software aimed to create an interface for entering detection input parameters, to make raster moves with the camera along the "zig-zag" trajectory, and to process all captured images by the developed image algorithm. Lastly, with a help of artificial intelligence the size, the position, and type of found objects are measured and written to the final list of defects. This list is then represented in the graphical user interface by spots in the scheme of a wafer and by the Excel file. The whole system was named WaferScan.

Finally, a set of experimental measurements was performed to evaluate the results.

In the first measurement, the results of analyzing the same wafer by the manual method on the metallograph by Mr. Král and the automated method performed by the Wafer-Scan were compared. The software method found more than 3× more defects than the manual method in the same zone.

In the following measurements, it was examined whether the system introduces defects into the measured sample. Fifteen consecutive measurements were performed and it was found that during the 2 hours only 2 defects fell on the measured sample. In the same measurement, it was also examined whether the measured data corresponded to the actual position of the defect on the wafer. Three defects found by the WaferScan were selected and found by the manual method. The comparison of the positions were on the order of millimeters.

Due to this inaccuracy, another measurement was performed with an improved wafer holder and updated software, where an error was found that was at maximum equal to the size of the field of view. The calibrating cross had already developed and applied during this measurement. From the data set that was measured in 5 consecutive measurements, one defect was tracked and compared with the results from the last, erroneous measurement and a real position of the defect. This measurement was more accurate than the previous one and the biggest inaccuracy was in the position of the defect which was 0.4mm.

The last measurement was performed to measure if the ambient light had any effect on the measured data. Two images were taken, one with ambient light, the other without it, and then correlated by a Matlab function "corr2". The correlation was measured to be 98 % and was effected not only by the elimination of the light but also by a small movement that was introduced during the covering of the system.

The option to upgrade the performance of the system is to add a tube next to the LED ring that would blow on the area before the photo was taken. This would lead to measuring only the defects that are in the layer of the polymer. Next option is to make a firmer holder of the camera. The one in use is 3D printed from plastic and shakes slightly even with gentle movements of the system.

Bibliography

[1] HU, Wenchuang, et al. Sub-10 nm electron beam lithography using cold development of poly (methylmethacrylate). Journal of Vacuum Science Technology B: Microelectronics and Nanometer Structures Processing, Measurement, and Phenomena, 2004, 22.4: 1711-1716.

[2] KNÁPEK, A., et al. Automated System for Optical Inspection of Defects in Resist-coated Non-patterned Wafer. Jordan Journal of Physics, 2020, 13.2: 93-100.

[3] DROZD, Michal. Návrh automatizované aparatury určené pro inspekci křemíkových desek ovrstvených PMMA [online]. Brno, 2020 [cit. 2022-03-19]. Accessible from:: https://www.vutbr.cz/studenti/zav-prace/detail/140771. Bakalářská práce. Vysoké učení technické v Brně, Fakulta strojního inženýrství, Ústav fyzikálního inženýrství. Vedoucí práce Alexandr Knápek.

[4] MATĚJKA, František. Praktická elektronová litografie. Ústav přístrojové techniky AV ČR, 2013.

[5] KHOURY, Maroun; FERRY, David K. Effect of molecular weight on poly (methyl methacrylate) resolution. Journal of Vacuum Science & Technology B: Microelectronics and Nanometer Structures Processing, Measurement, and Phenomena, 1996, 14.1: 75-79.

[6] CUMMING, D. R. S., et al. Fabrication of 3 nm wires using 100 keV electron beam lithography and poly (methyl methacrylate) resist. Applied physics letters, 1996, 68.3: 322-324.

[7] TSENG, Ampere A., et al. Electron beam lithography in nanoscale fabrication: recent development. IEEE Transactions on electronics packaging manufacturing, 2003, 26.2: 141-149.

[8] THOMPSON, L. F.; STILLWAGON, L. E.; DOERRIES, E. M. Negative electron resists for direct fabrication of devices. Journal of Vacuum Science and Technology, 1978, 15.3: 938-943.

[9] SAHU, Niranjan; PARIJA, B.; PANIGRAHI, S. Fundamental understanding and modeling of spin coating process: A review. Indian Journal of Physics, 2009, 83.4: 493-502.

[10] NANO™PMMA and Copolymer, MicroChem, [online], [cit. 2022-05-11].
Accessible from:
https://kayakuam.com/wp-content/uploads/2019/09/PMMA_Data_Sheet.pdf

[11] LALOVA, A.; TODOROV, R.; MALINOWSKI, A. J. Optical properties of thin PMMA films for sensor application. Bulg. Chem. Commun, 2015, 47: 29-34.

[12] WHYTE, William. Cleanroom technology: fundamentals of design, testing and operation. John Wiley & Sons, 2010.

[13] NEGRUTIU, Meda Lavinia, et al. Defectoscopy of denture polymers. Mater Plast Elastomeri Fibre Sint, 2012, 49.2: 129-132.

[14] MOHAMMED, Azad; ABDULLAH, Avin. Scanning electron microscopy (SEM): A review. In: Proceedings of the 2018 International Conference on Hydraulics and Pneumatics—HERVEX, Băile Govora, Romania. 2018. p. 7-9.

[15] HANNEMANN-MANTALAS, Lynda C.; LEVINSON, Harry J. Semiconductor process control. In: Handbook of Critical Dimension Metrology and Process Control: A Critical Review. International Society for Optics and Photonics, 1994. p. 102740E.

[16] RUGAR, Daniel; HANSMA, Paul. Atomic force microscopy. Physics today, 1990, 43.10: 23-30.

[17] DAI, Gaoliang, et al. Fast and accurate: high-speed metrological large-range AFM for surface and nanometrology. Measurement Science and Technology, 2018, 29.5: 054012.

[18] Magnification and resolution, Science Learning Hub, The University of Waikato [online], [cit. 2022-04-02]. Accessible from:
http://www.sciencelearn.org.nz/Contexts/Exploring-with-Microscopes/Science-Ideas-and-Concepts/Magnification-and-resolution

[19] ZERNIKE, Frits. Phase contrast, a new method for the microscopic observation of transparent objects. Physica, 1942, 9.7: 686-698.

[20] The Nobel Prize in Physics 1953, NobelPrize.org, Nobel Prize Outreach AB 2022 [online], [cit. 2022-04-06]. Accessible from:
https://www.nobelprize.org/prizes/physics/1953/summary/

[21] LACEY, Alan J. (ed.). Light microscopy in biology: a practical approach. OUP Oxford, 1999.

[22] Controller Area Network (CAN) Overview, National Instruments Corp. [online], [cit. 2022-04-21]. Accessible from: https://www.ni.com/cs-cz/innovations/white-papers/06/controller-area-network–can–overview.html

[23] CHEN, Yifang. Nanofabrication by electron beam lithography and its applications: A review. Microelectronic Engineering, 2015, 135: 57-72.

[24] LAWSON, Richard A.; ROBINSON, Alex PG. Overview of materials and processes for lithography. In: Frontiers of Nanoscience. Elsevier, 2016. p. 1-90.

[25] SINGH, Jitendra P., et al. Fabrication of magnetic tunnel junctions. In: Advanced Applications in Manufacturing Enginering. Woodhead Publishing, 2019. p. 53-77.

[26] KOCH, Christian; RINKE, Titus J. Photolithography: Basics of Microstructuring. MicroChemicals GmbH, 2017.

[27] THOMS, Stephen. Electron beam lithography. CRC Press, 2012.

[28] corr2 – 2–D correlation coefficient, The MathWorks, Inc., [online], [cit. 2022-05-14]. Accessible from: https://www.mathworks.com/help/images/ref/corr2.html

List of Symbols, Physical Constants, and Abbreviations

n .... refractive index

λ .... wavelength

M .... molar weight

ω .... spin speed

c .... concentration of the solution

k_η .... constant that includes viscosity and parameters of the spin coater

l .... length

k .... dispersion of the extinction coefficient

R .... angular resolution

NA .... numerical aperture

EBL .... Electron Beam Lithography

ISI CAS ...... Institute of scientific instruments of the Czech Academy of Science

PMMA .... polymethyl methacrylate

COP .... ethyl acrylate

ISO .... Organisation for Standardization

SEM .... Scanning Electron Microscope

AFM .... Atomic Force Microscope

VLM .... Visible Light Microscope

LED .... Light-Emitting Diode

USB .... Universal Serial Bus

VDC .... Volts of Direct Current

CMOS .... Complementary Metal–Oxide–Semiconductor

CAN .... Controller Area Network

ASCII .... Standard Code for Information Interchange

GUI .... Graphical User Interface

List of Tables

2.1 Airborne particulate cleanliness classes for cleanrooms standardized by ISO [12] . . . 9

3.1 Tracking of two defects in 15 consecutive scans . . . 27
3.2 Tracking of two defects before and after the upgrade of the device . . . 29

List of Figures

1.1 The manual setup for the inspection of the defects used in ISI CAS . . 4

2.1 A schematic diagram for one repeat unit of PMMA and one of its generic reaction path [7]. 5
2.2 A wafer with a PMMA film layer, with an approval from Ing. Stanislav Krátký, Ph.D. 6
2.3 A wafer with an inhomogenous film of resist [2] 7
2.4 The dependence of the refractive index on the thickness of thin spin-coated PMMA films at a wavelength of 600 nm [11]. 8
2.5 The Fiber defect appeared in the resist during the process of spin coating. The resist flake appeared in the resist during the process soft-baking. . 9
2.6 Defects caused by micro bubbles [2] 10

3.1 WaferScan, a measuring system 13
3.2 A model of a 4-inch wafer holder created in *Solidworks 2020* 14
3.3 A chart of electronic devices and communication canals 15
3.4 Cropped images of the standard captured by the optical setup of the WaferScan 16
3.5 A visualization of distortion of the optical setup 17
3.6 A flow chart of the Main function algorithm 18
3.7 The standard CAN frame format 18
3.8 The graphical user interface of the WaferScan application 19
3.9 The blue line is the “zig-zag” trajectory, the red square is the user-desired zone and the green lines show the overlap of the images 21
3.10 The image before and after the thresholding 22
3.11 Measurement of the size, position, and type of the defects; red boxes surround dust particles and blue boxes surround fibers 23
3.12 Images that are used for a correlation function “corr2” 24
3.13 Results of the measurement of the number of particles in the room . . . 25
3.14 Results of the first measurement 25
3.15 The number of found defects in 15 consecutive scans 26
3.16 Three defects detected by the software (red crosses) and by hand (blue crosses) 28
3.17 Correlated images taken with and without ambient lighting 30